Optics and Lasers in Engineering 143 (2021) 106624

Contents lists available at ScienceDirect

Optics and Lasers in Engineering

journal homepage: www.elsevier.com/locate/optlaseng

Optimization analysis of partially coherent illumination for refractive index tomographic microscopy

Jiaji Li [a,b,c], Ning Zhou [a,b,c], Zhidong Bai [a,b,c], Shun Zhou [a,b,c], Qian Chen [a,b], Chao Zuo [a,b,*]

[a] School of Electronic and Optical Engineering, Nanjing University of Science and Technology, No. 200 Xiaolingwei Street, Nanjing, Jiangsu Province 210094, China
[b] Jiangsu Key Laboratory of Spectral Imaging & Intelligent Sense, Nanjing University of Science and Technology, Nanjing, Jiangsu Province 210094, China
[c] Smart Computational Imaging Laboratory (SCILab), Nanjing University of Science and Technology, Nanjing, Jiangsu Province 210094, China

ARTICLE INFO

Keywords:
Computational microscopy
Three-dimensional imaging
Diffraction tomography
Signal processing

ABSTRACT

Partially coherent optical diffraction tomography (PC-ODT) is a well-established label-free quantitative three-dimensional (3D) imaging technique based on the refractive index (RI) contrast by measuring the intensities at multiple axially displaced planes. The imaging performance of tomographic RI microscopy is determined by the inversion of phase optical transfer function (POTF) which depends on the illumination pattern of imaging system. Here, we propose the optimization analysis of illumination pattern in PC-ODT, and the custom-build quantitative criterion is demonstrated to maximize the performance of POTF related to the “goodness” evaluation of an illumination aperture. Source modulation with different segment scale and gray scale is implemented to acquire arbitrary distribution source, and the corresponding 3D POTF can be easy obtained through the numerical incoherent superposition of each segment components. Moreover, the metrics of 3D POTF for various illuminations over the condenser aperture are analyzed. We test the obtained optimal illumination by imaging both a simulated micro phase bead and a real control bead sample, suggesting superior performance over other suboptimal patterns in terms of both SNR and spatial resolution. Further, experimental result based on unstained MCF-7 cell clusters is presented support this finding as well, and the proposed method is expected to find versatile applications in biological and biomedical research.

1. Introduction

Optical diffraction tomography (ODT) is a wide-field label-free three-dimensional (3D) refractive index (RI) imaging technique enabling attractive imaging modality for studying weakly absorbing samples like microorganisms and cells [1–4]. Alternative to exogenous 3D labeling methods (e.g., fluorophores) in confocal [5] and two-photon fluorescence microscopy [6], 3D RI distribution of the specimen recovered by diffraction tomography makes it possible to calculate important quantitative information such as volume, surface area, dry mass and other related characteristics without photobleaching, phototoxicity, and other artificially damaging effects [7–10]. The most widely used interferometric-based RI tomographic techniques is coherent ODT (C-ODT) employing the existed holographic microscopes and spatially coherent laser illumination [11–13]. Several angle scanning [11–18] or object rotation [19,20] approaches have been invoked in C-ODT. Then, the computerized tomography or diffraction tomography algorithm based on the Fourier diffraction theorem [21–23] is applied to the reconstruction of 3D RI by assembling numerous sections of the object spatial spectrum obtained for each illumination directions.

On the other side, without the implementation of interference optical path, the diffraction tomography can also be realized by the intensity recording based on a conventional bright-field microscope under coded illumination schemes [24–28]. Under the situation of 3D RI tomography without axial mechanical scanning, the diverse source illumination is invoked to the 3D imaging process, and a multi-slice imaging-based model is proposed to performs 3D synthetic aperture using a robust computation and memory efficient slice-wise deconvolution algorithm for incoherent resolution limit [29–35]. Moreover, the technique of Fourier ptychographic diffraction tomography is introduced by employing iterative procedure like FPM but in 3D space to reconstruct 3D RI of object [24,36–38].

By utilizing the axial focus scanning, the partially coherent optical diffraction tomography (PC-ODT) can be realized under the partially coherent illumination or diverse illumination[25,26,39–43], and the 3D RI distribution is directly recovered through the deconvolution between 3D phase optical transfer function (POTF) and a stack of through-focus intensity images. Recent studies have found that the shape of the illumination aperture has a significant impact on the resolution and quality of 3D RI tomography, and by simply replacing the conventional circular illumination aperture with an annular one or Gaussian one, the quality of

* Corresponding author.
E-mail addresses: jiajili@njust.edu.cn (J. Li), zuochao@njust.edu.cn (C. Zuo).

https://doi.org/10.1016/j.optlaseng.2021.106624
Received 3 January 2021; Received in revised form 8 March 2021; Accepted 15 March 2021

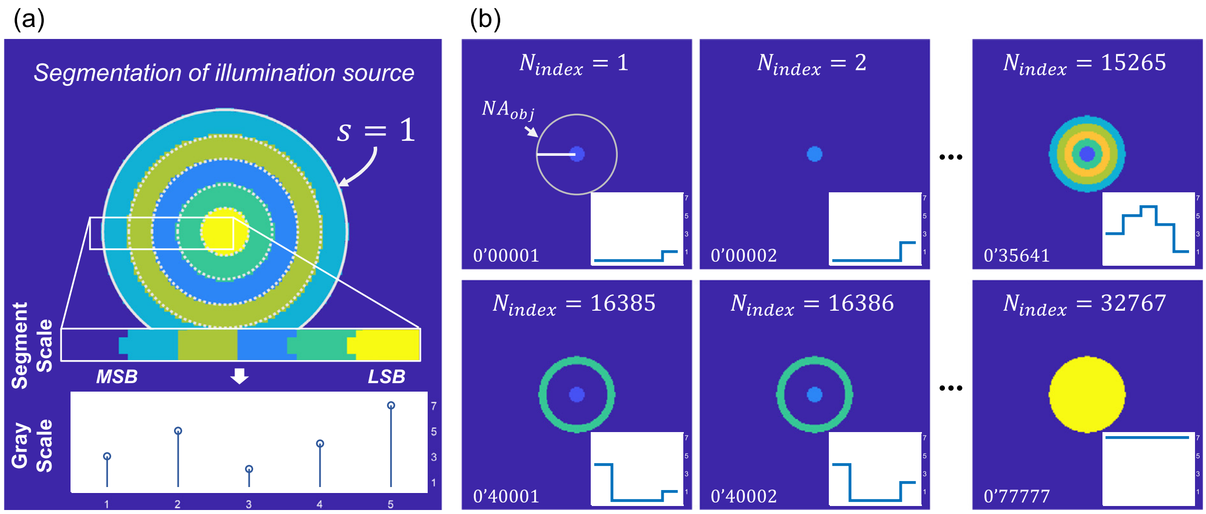

Fig. 1. Gray scale segmentation of illumination source and labeling of all combinatorial illumination patterns. The incoherent illumination source is evenly divided into a lot of discrete annular patterns with same center point, and these annuli are labeled from the LSB to the MSB with 5-Bit segment scale and 3-Bit gray scale. The radius cut-profile of each illumination pattern is illustrated as a digital wave of analog to digital converters, and the corresponding illumination pattern can be numbered from 1 to 32767 in decimal (from 0'00001 to 0'77777 in octal).

imaging result is significantly enhanced [28,32,44–48]. Above existed tomographic approaches provide fast non-interferometric speckle noise-free imaging in conventional wide-field microscopes, and various coded partially coherent illumination schemes for 3D RI imaging are investigated as well. However, PC-ODT still suffers from the mainly principal inconveniences of serious missing cone problem and bad signal to noise ratio (SNR) of RI reconstruction due to the incomplete Fourier coverage of POTF. And the annular or Gaussian aperture in the previous work is empirically designed based on intuitive criteria related to the shape of POTF, which does not guarantee optimality. Besides, the analytically optimized POTF is only focused on Gaussian illuminations (GIs) in [49] instead arbitrary non-uniform illumination pattern containing high order polynomial term.

In this work, we investigate the imaging performance of 3D POTF under the single arbitrary illumination aperture with the deconvolution of intensity stack. We consider numerical segment division of illumination source and a balanced distribution criterion for the evaluation of POTF is proposed as well. As illustrated in Fig. 1, the source modulation is implemented with different segment scale and gray scale to obtain arbitrary distribution source using custom-printed circular film flakes located on the condenser diagram aperture. The pre-designed patterns are printed on the photographic film, and the diameter size of these circular film flakes with the opaque region matches the objective pupil in the back focal plane exactly. Each combined 3D POTF can be calculated through the incoherent superposition of segment components, and the POTF's imaging performance of corresponding illumination source is evaluated by custom-designed metrics. Further, the POTF with the best metrics is chosen as the optimal one among all combinations of illumination patterns, and we draw the conclusion that the theoretical optimality of annular illumination over all patterns (including arbitrary circular and Gaussian patterns) in the numerical segmentation strategy.

Although the similar works invoking binary annular illumination and GI patterns have been empirically proposed to enhance the imaging resolution and alleviate the incomplete 3D Fourier space coverage of POTF in tomographic microscopy [44,50,51], the optimality of these apertures among various partially coherent illumination patterns has not been demonstrated yet. Recent works give a closed-form integral expression for the POTF under various illumination objective pupils enabling rapid calculation of the POTF [47], and the analytical optimization analysis POTF for Gaussian illumination is developed [49]. Nevertheless, in the case of both of analytical expression and corresponding analytical forms of POTF are not available for extremely complex distributed source pattern, we still need to employ numerical integral to calculate the distribution of POTF.

Overall, the novelty of this work is to estimate the quality of 3D POTF quantitatively through numerical metrics for arbitrary gray scale pattern instead of empirically designed illumination pattern, and the optimal analysis of partially coherent illumination is proposed in the single through-focus intensity stack-based diffraction tomographic imaging. Besides, we analyze different types of illumination to improve the homogeneity of 3D POTF and get better intensity response distribution across the spatial cutoff frequency coverage (SCFC) validating the viability of PC-ODT technique in the proposed manuscript. Even thought this kind of numerical illumination segmentation strategy seems indecent, the problem of POTF calculation can be easily solved by a discrete processing for the case of complex continuous pattern distribution, which is analogy to the convert of analog signal to digital signal using an Analog to Digital Converters (ADC) for commonly signal data processing purposes. Finally, the 3D RI reconstruction results based on a simulated 3D pure phase micro sphere are proposed under different illumination apertures for the comparative quality of 3D POTF. And the numerical simulations confirm the performance of these optimization analysis and support the introduced balanced distribution criterion. Finally, the experimental comparative result based on control bead sample and unstained biological cell basically validate the optimization analysis of POTF, and this pave the way to high resolution and high quality 3D RI tomography in a conventional microscope for biomedical imaging.

2. Principle and methods

2.1. 3D POTF for arbitrary gray scale illumination source

For the diffraction tomography in a partially coherent microscope, the optical scattering potential related to 3D object permittivity is encoded into the axial recorded intensity stack. The scattering potential function of object can be written as $V(\mathbf{r}) = k_0^2\left[n^2(\mathbf{r}) - n_m^2\right]$, where k_0 is the wave number $2\pi/\lambda_0$ with λ_0 being the wavelength in free-space, $n(\mathbf{r})$ and n_m are the RI of object and immersion medium, correspondingly. The complex RI $n_p(\mathbf{r}) + i \cdot n_a(\mathbf{r})$ contains phase component n_p in real part and the absorption component n_a in imaginary part, respectively. The scattering potential is almost always a real function due to the invoking of pure phase or weakly absorbing approximation in the experiments. In the partially coherent illumination field, image formation of 3D object can be interpreted as the 3D convolution between the object and point spread function (PSF) of system by employing the weak scattering approximation (Born approximation) [22,23]. By ignoring high order scattering components, the recoded 3D intensity image stack can be expressed as a linear sum of the real and imaginary parts of the object scattering potential convolved with the corresponding PSFs $H_P(\mathbf{r})$ and $H_A(\mathbf{r})$, and the corresponding product equations in Fourier space by implementing 3D fast Fourier transform (FFT) are:

$$I(\mathbf{r}) = B + \Phi(\mathbf{r}) \otimes H_P(\mathbf{r}) + A(\mathbf{r}) \otimes H_A(\mathbf{r}), \tag{1}$$

and

$$\widetilde{I}(\zeta) = B\delta(\zeta) + \widetilde{\Phi}(\zeta)T_P(\zeta) + \widetilde{A}(\zeta)T_A(\zeta), \tag{2}$$

respectively. Where B is the background intensity or DC term in frequency space, and it can be understood as the un-scattered light or transmitted light, $\Phi(\mathbf{r})$, $A(\mathbf{r})$, $\widetilde{\Phi}(\zeta)$, and $\widetilde{A}(\zeta)$ are the respective real and imaginary parts of object scattering potential function and corresponding frequency spectrum, $T_P(\zeta)$ and $T_A(\zeta)$ are the POTF and amplitude optical transfer function (AOTF), respectively.

N. Streibl [39] derived the analytical integral form of 3D optical transfer function (OTF) in a bright-field microscope by considering the first-order Born approximation (weak scattering object) in the paraxial regime. As well, Y. Bao *et al*. [43] given the analytically explicit equation of 3D OTF under non-paraxial approximation. More recently, J. Huang *et al*. [47] report the analytical version of 3D POTF integration formula for different illumination designs (including GI and annular illumination). Thus, the complicated derivation of 3D OTF is skipped here, and the completely analytical form of 3D POTF can be found in the content of [43,47]. However, above-mentioned works only focus some commonly used uniform and non-uniform illumination sources (circular illumination, Gaussian illumination, and annular illumination etc.), and it is not easy to calculate the numerical integration expression of analytical 3D POTF for arbitrary illumination pattern, especially for some non-uniform illuminations containing high order polynomial term [49]. On the other side, T. Noda *et al*. proposed 3D tomographic method cooperated with annular illumination, and the numerical integration of 3D POTF is available for the annular patten [52,53]. Due to the incoherent superposition of intensity contribution arising from all coherent points on the source plane, 3D POTF of annular patten with arbitrary outer and inner radius can be calculated. The expression for arbitrary annular illumination aperture can be defined as follows:

$$S_i(\rho)=\begin{cases} 1, & if\ \rho_{i-1} < |\rho| \le \rho_i \\ 0, & else \end{cases} \tag{3}$$

Where ρ_{i-1} and ρ_i represent the normalized frequency of inner and outer radius of corresponding annular illumination pattern. By implementing the annular discretization to incoherent source pattern, the 3D POTF of corresponding illumination pattern can be calculated through the numerical integration of transfer function for each individual point source on the aperture plane. As shown in Fig. 2, the incoherent circle illumination source is evenly divided into a lot of discrete annular patterns with same center point and width expecting for different segment bit-depth, and each corresponding 3D POTF can be obtained through the numerically integration. Fig. 2 illustrates the 2D plots of 3D POTF sections in $u-w$ plane for annular illumination patterns with different segment bit-depth. Visualization 1 shows more details for the changing of illumination source and axially sectional distributions of 3D POTFs.

For the representation of arbitrary illumination source, we proposed the custom-designed source segmentation strategy to illustrate all source patterns with gray scale instead of binary one. Fig. 1 shows the segmentation of illumination aperture and labeling of all combinatorial gray scale illumination patterns. Incoherent illumination source ($s = 1$) is evenly divided into many concentric discrete annular illumination patterns with N_1 segment bit-depth, and these rings on the source plane are marked from the least significant bit (LSB) to the most significant bit (MSB), where the coherence parameter s is defined as the ratio of illumination NA to objective NA (NA_{ill}/NA_{obj}). Moreover, these discrete annular patterns with different inner and outer radius are varied within different gray levels with N_2 bit-depth, and each single annular illumination pattern can be labeled as a unique octal number, decimal number, hexadecimal number, or arbitrary bit-depth coded number. This illumination segmentation strategy is analogy to the convert of analog signal to digital signal using an ADC for data processing purposes. The annular segment sampling bit N_1 and gray scale bit-depth N_2 are 5-Bit and 3-Bit in Fig. 1, respectively. Thus, the maximum index number of coded gray illumination pattern is 32767 ($2^{N_1+N_2}-1$) in decimal number corresponding 0'77777 in octal number for 5-Bit segment bit-depth and 3-Bit gray scale bit-depth. The radius cut-profile of each pattern is plot as well just like the ADC coding wave, and the corresponding illumination aperture is labeled with a unique index number from 1 to 32767 in decimal code in Fig. 1. After the segmentation process, the arbitrary gray scale distribution source with can be obtained as the linear addition of single annular pattern from LSB to MSB, and the gray coded illumination source can be expressed as:

$$S_N(\rho) = \sum_{i=1}^{N_1} a_i S_i(\rho), a_i \in \left[0, 2^{N_2}-1\right] \cap (\mathbb{Z})^+ \tag{4}$$

where N is the index of arbitrary gray illumination pattern, a_i is the gray scale weight of each single divided annular pattern ranged from 0 to $2^{N_2}-1$. This expression demonstrates the intensity distribution of any non-uniform axially symmetric illumination sources can be accurately superposed by a series of annular shape apertures. Since the individual contributions of each annular sources component in Fig. 2 and the linear superposition of POTF integration with respect to illumination intensity, the 3D POTF distribution for a given arbitrary illumination pattern $S_N(\rho)$ can be calculated through incoherent linear combination of corresponding annular patten's POTF contribution.

This segmentation strategy of illumination source is invoked to create a single non-uniform illumination pattern projected at the condenser's back focal plane, and this approach allows the OTF calculation for arbitrary gray illumination patterns whose analytical OTF expressions is not available. Moreover, the optimal illumination aperture with the best 3D imaging performance can be founded among all combinatorial gray scale patterns instead of empirically designed illumination pattern. The segmentation and labeling of all combined illumination patterns make it is easier to calculate the POTF of corresponding source pattern and provide a numerical analysis basis for optimizing of 3D POTF in PC-ODT.

2.2. Performance evaluation of 3D POTF

The numerical segmentation and coding make the 3D POTF calculation of arbitrary illumination source easy using the incoherent superposition of corresponding annular patterns' POTF contribution, but the evaluation of 3D POTF performance is still a hard task. In contrast to the isotropic distribution of 2D imaging system TFs along transverse direction, the SCFC region of 3D POTF of proposed illumination sources is a boundary shape instead of a certain frequency point value due to the anisotropy of 3D POTF along lateral and axial directions. However, the 3D POTF distribution of corresponding illumination aperture is symmetrical along z axis, and we just need to analyze the axial section of 3D POTF in $u-w$ plane, as shown in Fig. 2. In the previous works [44,51], the histogram statistics of POTF has been proposed for the quantitative analysis of imaging performance of POTF. Here, a custom-designed criterion is developed for the quality evaluation of 3D POTF to find the optimal aperture among all arbitrarily combined sources. Three metrics are given for the quality of 2D sections of POTF as following: 1) The ratio of cutoff frequency coverage to theoretical incoherent POTF frequency coverage should be large. In other words, the non-zero region of POTF should be as large as possible. 2) The ratio of non low value

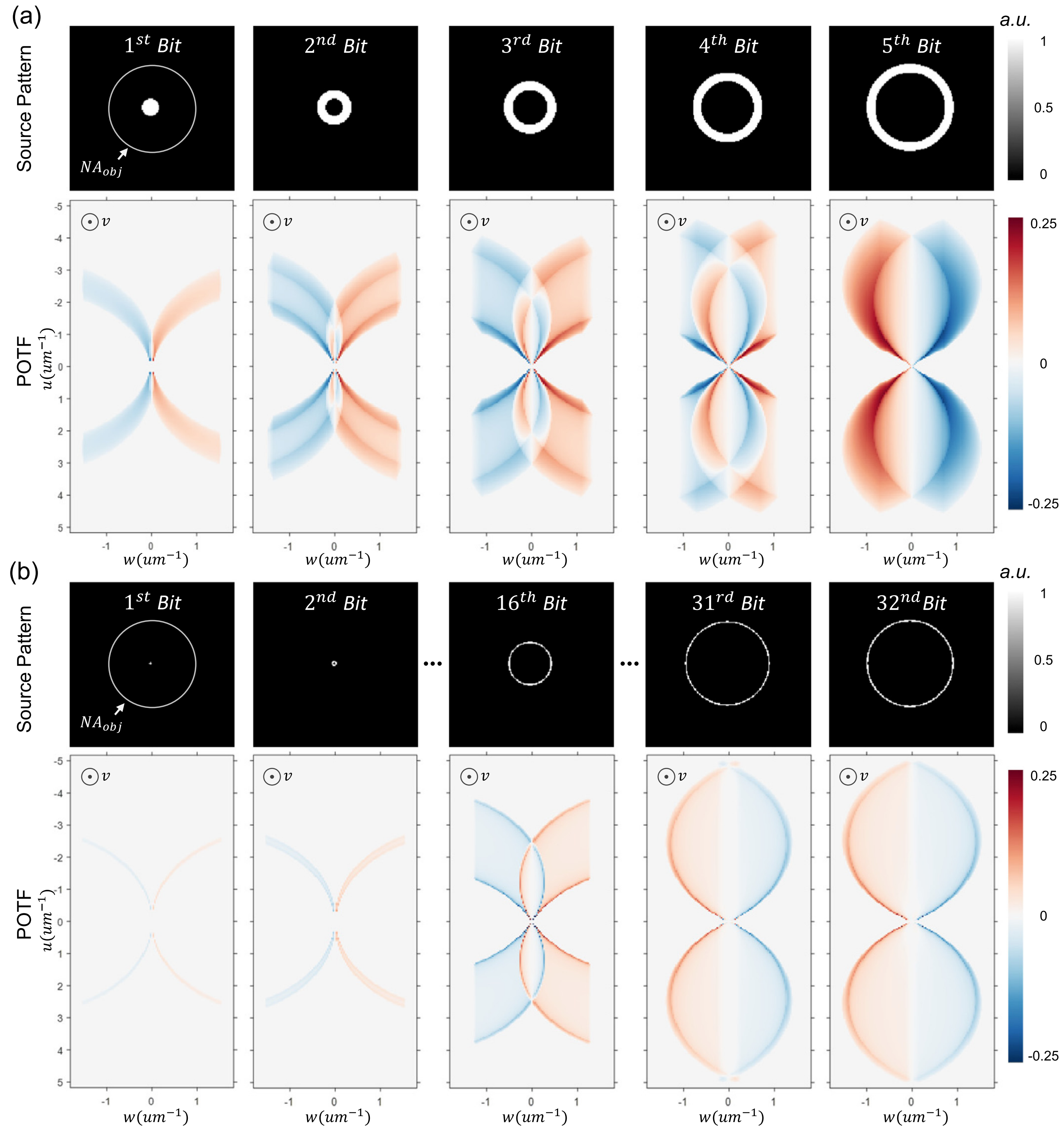

Fig. 2. 3D POTF sections of annular shape apertures with (a) 5-Bit and (b) 32-Bit depth segmentation of incoherent illumination source. Visualization 1 and Visualization 2 shows more details for the change of illumination source and axially sectional distributions of 3D POTFs.

(non-LV) region coverage to theoretical incoherent POTF frequency coverage should be large as well. The frequency response of corresponding POTF with almost negligible absolute values is defined as as LV region, and the LV region in the whole frequency pass-band may alter the spatial imaging resolution and prevent the improvement of SNR of 3D RI reconstruction. 3) The absolute mean value of POTF among non-zero region should be as large as possible. The RI volume with better SNR can be recovered under the deconvolution of POTFs with larger absolute mean value. For the optimal case under these three metrics, the ideal POTF must have the smallest missing cone region, nonhomogeneous contrast for different spatial frequency regions, and the largest absolute mean value of modulus. Overall, above proposed metrics for 3D POTF evaluation are both empirically heuristic rules successfully utilized in the past pupil engineering field as rules of thumb. And the instructive cost function, can be evaluated for source pattern optimality, is expressed as following:

$$\arg\min_{S} \left\| |T_P(S)| - |T_{P0}| \right\|_2^2 \tag{5}$$

where $|T_P(S)|$ denotes the absolute distribution of POTF for a given arbitrary gray illumination pattern S, while $|T_{P0}|$ represents the ideal step transfer function enveloped in incoherent cutoff frequency region of 3D imaging system. The POTF with the most robust response over the whole incoherent pass-band are the optimal one, and the 3D phase information can be transferred to the intensity stack efficiently under the corresponding illumination aperture. Even though the detailed analytical cost function may not be given to evaluate the performance of POTF, the above mentioned three metrics are enough to find the corresponding optimal illumination aperture among all combination of patterns.

For example, a given gray-coded illumination pattern and corresponding POTF section in colormap are illustrated in Fig. 3(a) and 3(b1), respectively. Also, the radius cut-line of illumination source is plotted, and the index value can be labeled as a unique octal number or corresponding decimal number with 5-Bit segment scale and 3-Bit gray scale. The non-zero spatial frequency coverage region of POTF is displayed in binary mask in Fig. 3(b2), and the envelope of incoherent cutoff frequency (marked by red solid line) is given as well. Moreover, the cut-off frequency of POTF is marked with red dotted line and the non-LV region is illustrated in mask in Fig. 3 (c1) and (c2), correspondingly. The LV region is determined by the POTF absolute values below a cutoff threshold value of 0.1, and this threshold value is often empirically determined in the transfer function of imaging system analysis to achieve better SNR [44]. To obtain the optimal illumination pattern, we need to calculate the distributions of these three POTF metrics of all combined source apertures. First, the POTF cutoff frequency coverage ratio of all illumination patterns from the index 1 to 32767 can be calculated, and the illumination patterns with the maximum cutoff frequency value are kept, as depicted in Fig. 3(d). Next, the statistic of non-LV region coverage ratio to incoherent POTF frequency coverage are given in Fig. 3(e), and the source patterns with non-LV region coverage ratio less than 0.45 are filtered out. Then, the absolute mean value of filtered POTF with 0.8 cutoff frequency coverage ratio and 0.45 non-LV region coverage ratio is shown in Fig. 3(f), and these the source patterns with absolute mean value of POTF greater than 0.1 are retained for the optimal source apertures. Finally, as illustrated in Fig. 3(g), the index of POTF with the maximum mean value is corresponding to the best imaging performance obviously, and the corresponding illumination pattern is the optimal one under the metrics for POTF quality evaluation. Visualization 2 shows the changing of cutoff frequency coverage ratio, non-LV coverage ratio, and mean value of transfer function with the increasing of source pattern index in a part of selected range. Overall, the optimal illumination pattern is the biggest single annulus and the corresponding POTF with the best imaging performance can be available for 3D RI tomography. It is interesting that the annular illumination patterns with same segmentation distribution but different gray level (e.g., 0’10000 and 0’20000 etc.) provide the same imaging performance. This phenomenon means that the absolute brightness of illumination source does not affect the response of system POTF, which is consistent with the situation of brightness of source will not determine the response of transfer function in actual microscopic imaging system. Moreover, only patterns that are primarily composed of the outer annulus will ever be determined to be optimal one using our proposed evaluation metrics because the highest imaging resolution is just contributed from the the outer annular aperture.

2.3. Effect of segment and gray bit-depth

In this subsection, we will take the different degrees of discretization of illumination source into consider, and the effect of bit-depth between segment and gray scale to the 3D POTF of arbitrary illumination patterns is discussed. The statistics of 3D POTF metrics corresponding 5-Bit segment scale with 3-Bit gray scale, 6-Bit segment scale with 3-Bit gray scale, and 5-Bit segment scale with 4-Bit gray scale are evaluated in Fig. 4, respectively. As illustrated in Fig. 4(a), for the SCFC, all source patterns are always equally divided into $2^{N_2}-1$ parts in spite of different segment bit-depth invoked, and the width of maximum cutoff frequency region of each parts is 0′777 (with N_1-2 Bits). Start and end index of source pattern with maximum cutoff frequency are regularly marked and given in Fig. 4(a) as well. It can be concluded from Fig. 4(a) that the increasing of segment scale will improve the SCFC ratio. It reveals that the annular illumination with narrower width can provide better cutoff frequency coverage ratio, coincident with the conclusion in quantitative phase imaging [50]. However, the increasing of gray scale bit-depth does not change the cutoff frequency coverage ratio since the spatial size parameter of annular illumination is not been changed. Then, the non-LV coverage ratio of all source patterns are presented in Fig. 4(b), and two sub-regions for these three different pattern segmentation strategies are chosen for the comparison. From the overall trend of non-LV coverage ratio, the POTFs with same segment bit-depth has the similar distribution but with more jitter and details. This result reflects that more segment bits can represent illumination source with finer pattern combinations, but it does not change the trend of non-LV coverage ratio. The enlarged sub-regions of non-LV coverage are shown in Fig. 4(c)-(e). As the arrows marked, these peak values are corresponded to the local maximum value, and the local maximum values are gradually decreased due to the offset of POTF contribution from the inner annular pattern. Fig. 4(c2)-(e2) show the similar trend of gradually decreasing with enlarged windows. Especially, the annular source patterns with octal index 0’8800 or hexadecimal index 0xEE000 are not included in the non-LV coverage because the cutoff frequency ratio of corresponding POTF is smaller than the maximum cutoff frequency ratio.

Next, the absolute mean value of POTFs are plotted in Fig. 5 as well. Similar to the above phenomenon, the POTF of corresponding annular illumination with more segment bit-depth has higher mean value. The increasing of gray scale bit-depth does not affect the distribution of mean value of POTF, and the POTF contribution of inner pattern will offset the POTF response from outer source. Thus, the annular pattern with the outermost ring shape has the best performance, and the optimal source aperture can be reached through the numerical analysis of arbitrary illumination pattern. Overall, the optimal illumination pattern is the biggest single annulus matched with objective pupil, and the annular width of pattern should be as small as possible.

In order to validate the effect of segment bit-depth on the final performance of 3D POTF, the POTF metrics of cutoff frequency coverage, non-LV coverage, and mean of value with different segment bit-depth but fixed 3-Bit gray scale are plotted in Fig. 6. We use 5-Bit, 6-Bit, 8-Bit, 12-Bit, and 16-Bit segment bit-depth to represent arbitrary illumination patterns, and the annular source patterns with the outermost ring index but different regermination bits (e.g., from 0’70000 to 0’76000 and from 0’700000 to 0’760000 etc.) are employed to compare the transfer function metrics with each other. Since the changing of gray scale bit-depth does not affect the final performance of POTF, only the annular patterns with local metrics peaks are compared in this section. For these source patterns under 8-Bit gray scale, the self-designed all metrics are increased, this mean that the annular illumination with narrower width can provide the most balanced ability POTF of 3D imaging system. The increasing gray value of inner annular shape will decrease the coverage ratio of non-LV and mean value of POTF. Overall, the basic trend of POTF metrics is getting better with more segment bits.

2.4. Characterization of 3D POTF for various illuminations

In order to characterize the 3D POTF for various illuminations, the POTFs of two typical partially coherent illumination schemes (including GI and annular illumination) are employed to compare with each other in this work. The imaging performance of various POTFs based on a simulate phase bead is evaluated under different illuminations. As proposed in previous works [44,47], the GI strategy is studied for the imaging quality improvement of 3D RI tomography using single stack data. Thus, we start the POTFs analysis by considering the typically GI and annular illumination. To represent the Gaussian source pattern, 32-

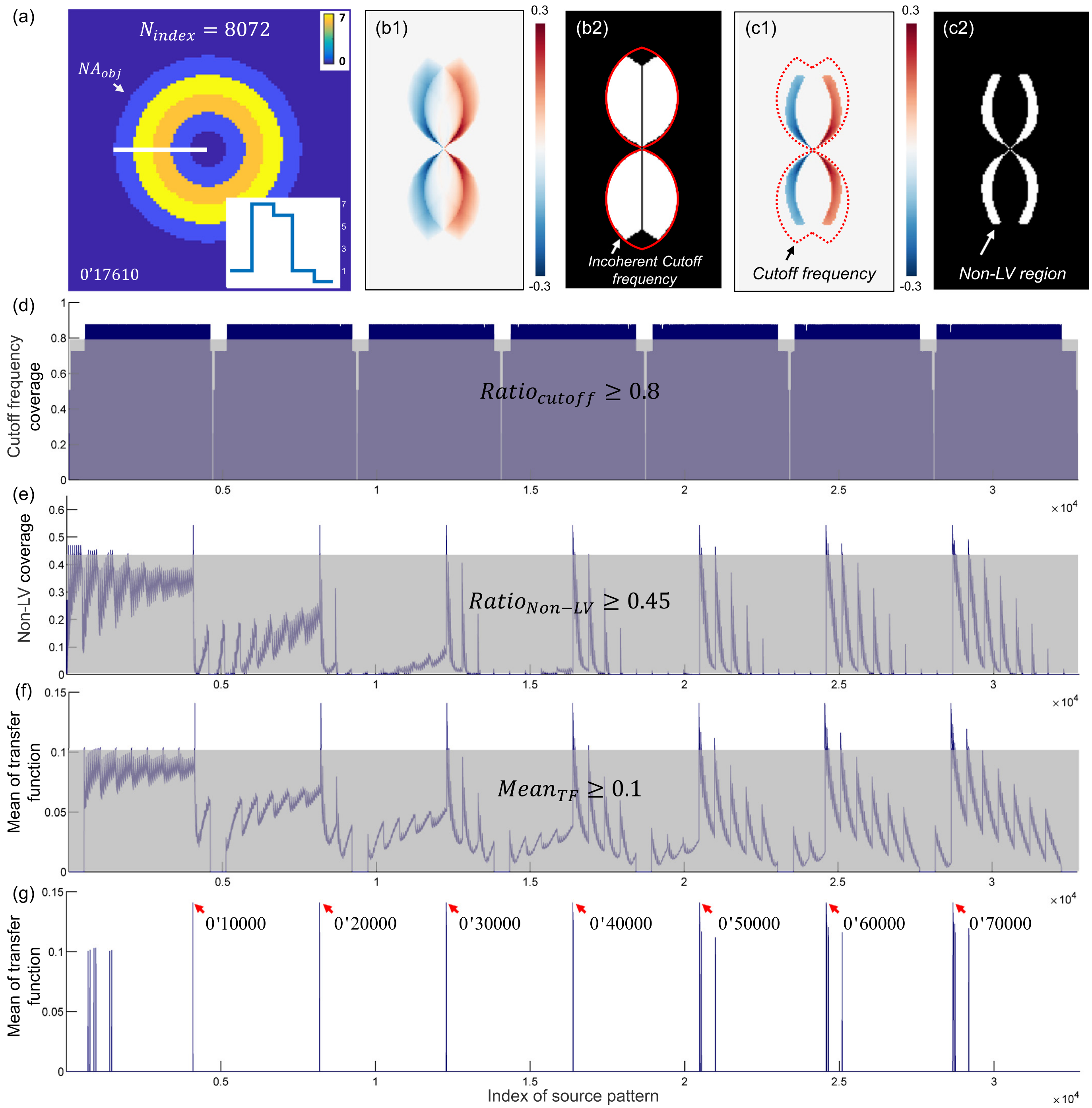

Fig. 3. Imaging performance evaluation of 3D POTF of all illumination source patterns using three crucial metrics, including cutoff frequency coverage, non-LV coverage, and mean value of transfer function. (a) Example of gray-coded illumination pattern. (b) Corresponding axial POTF section in colormap and the non-zero region of POTF in binary mask (Envelope of incoherent cutoff frequency marked by red solid line). (c) Cut-off frequency of POTF marked by red dotted line and the non-LV region in binary mask with cutoff threshold value of 0.1. (d) The cutoff frequency value of POTF of all illumination patterns is calculated and the illumination patterns whose cutoff frequency equals the maximum normalized cutoff frequency are retained. (e) Statistics of non-LV region coverage ratio of source patterns, and the filtered source patterns with non-LV region coverage ratio less than 0.45. (f) Absolute mean value of filtered POTF with 0.8 cutoff frequency coverage ratio and 0.45 non-LV region coverage ratio. Source patterns with absolute mean value of POTF greater than 0.1 are retained. (g) Index of POTF with the maximum mean value is corresponding to the best imaging performance (e.g., 0'10000 and 0'20000 etc.), and the corresponding illumination pattern is the optimal one under the metrics for POTF quality evaluation. With the increasing of source pattern index in a part of selected range, the changing of cutoff frequency coverage ratio, non-LV coverage ratio, and mean value of transfer function are plotted in supplementary Visualization 2.

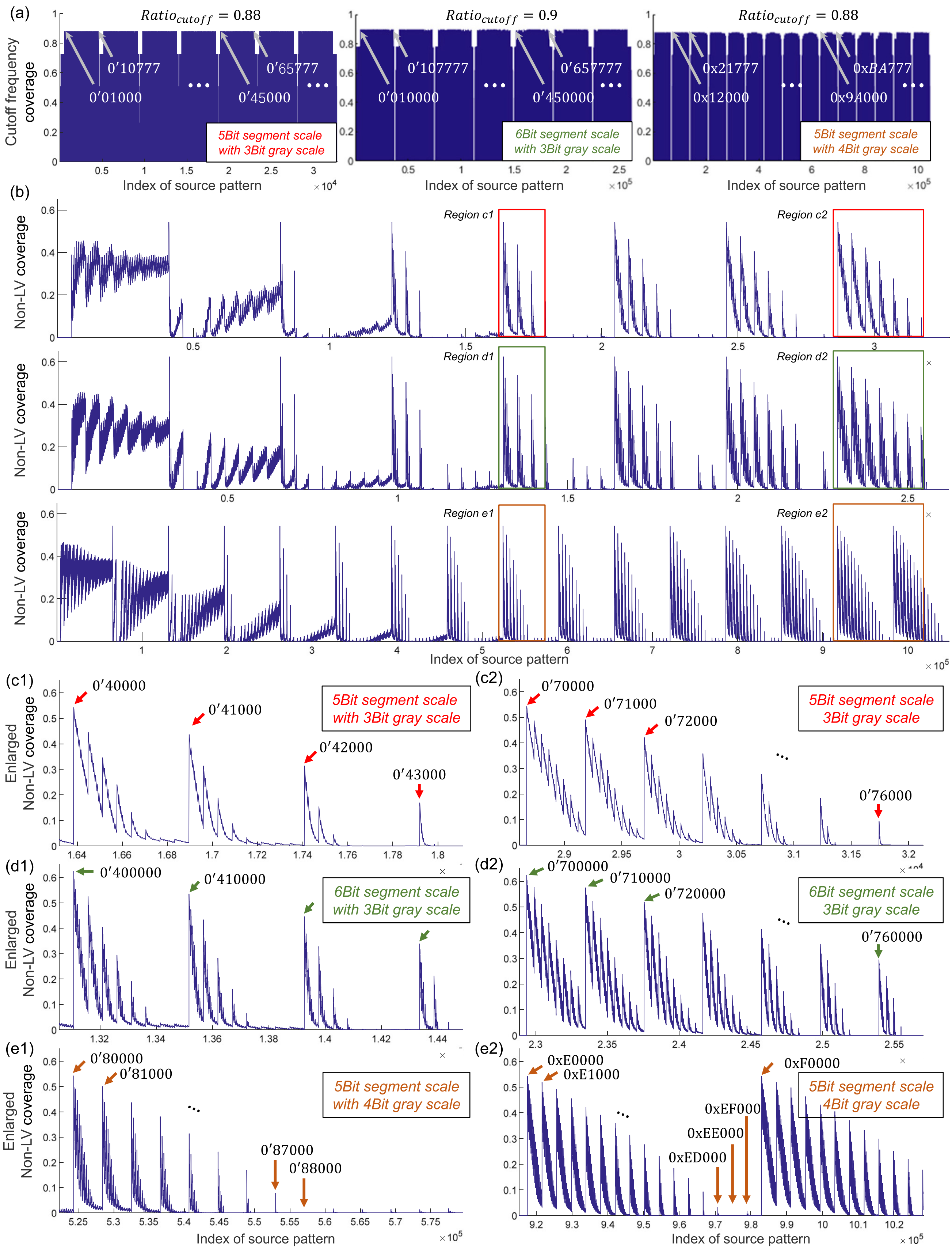

Fig. 4. The effect of source pattern segment and gray bit-depth on the POTF mercies of cutoff frequency coverage and non-LV coverage. Transfer function metrics comparison of cutoff frequency area and non-LV region with different source segment scale and gray scale. (a) Cutoff frequency coverage distribution of all combined source patterns with 5-Bit segment scale and 3-Bit gray scale, 6-Bit segment scale and 3-Bit gray scale, and 5-Bit segment scale and 4-Bit gray scale, correspondingly. (b) Non-LV coverage distribution of all combined source patterns with corresponding segment scale and gray scale. (c)-(e) Non-LV coverage of enlarged sub-regions in all source patterns index.

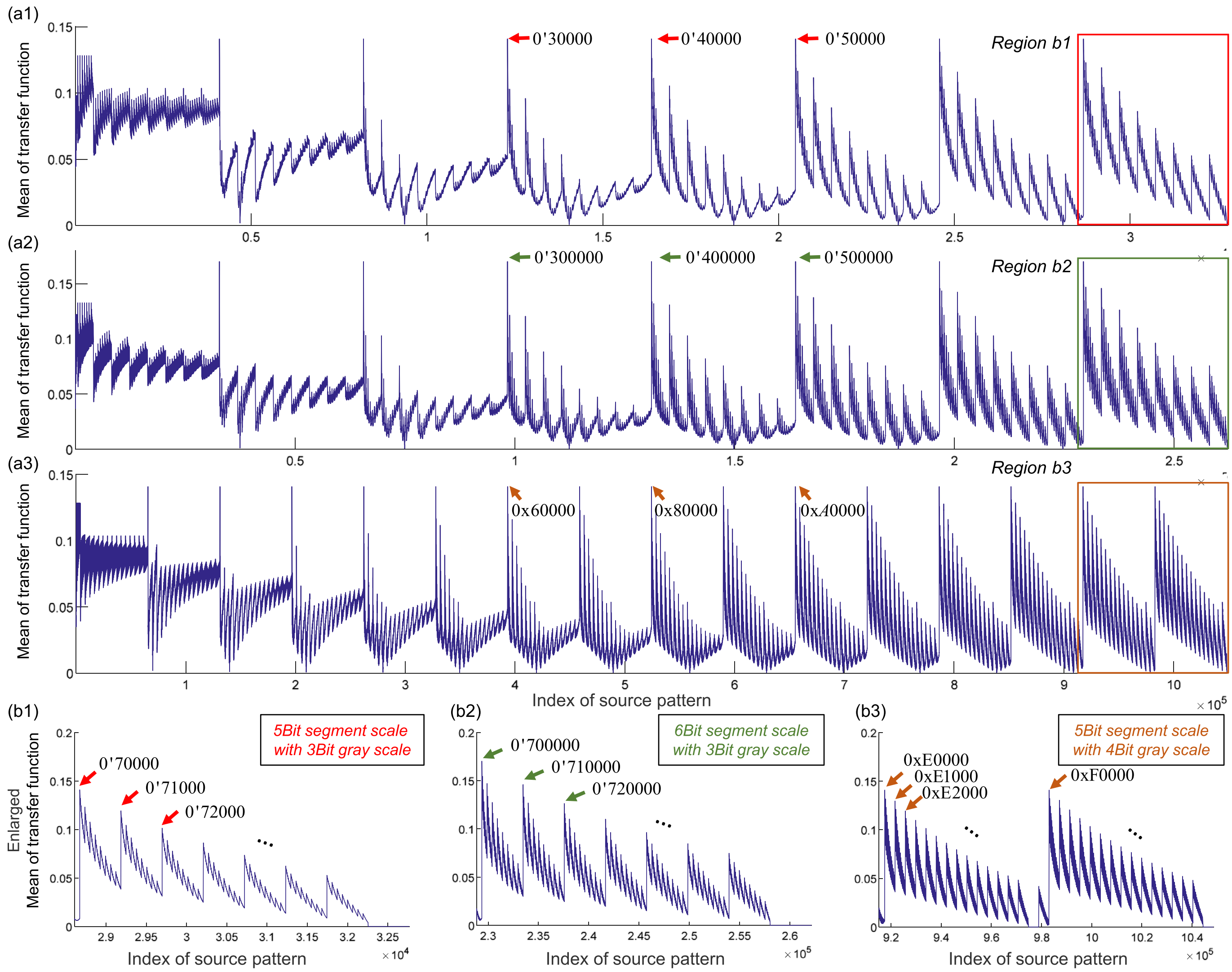

Fig. 5. The effect of source pattern segmentation and gray scale bit-depth on the POTF mercies of mean of transfer function. (a) Mean of POTF distribution of all combined source patterns with 5-Bit segment scale and 3-Bit gray scale, 6-Bit segment scale and 3-Bit gray scale, and 5-Bit segment scale and 4-Bit gray scale, restively. (b) Mean of POTF of enlarged sub-regions in all source patterns index.

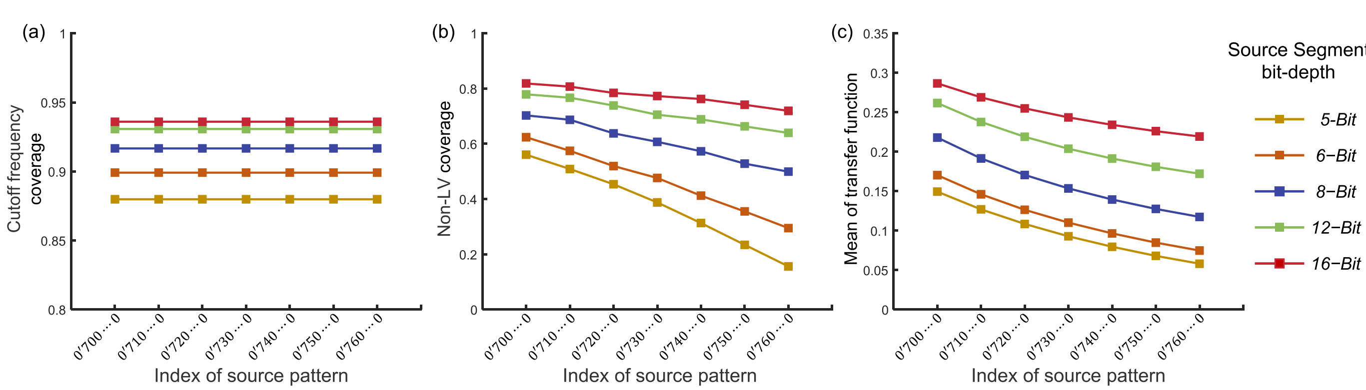

Fig. 6. POTF metrics of some special index of annular source patterns (e.g., from 0'70000 to 0'76000 and from 0'700000 to 0'760000 etc.) with different segment scale (5-Bit, 6-Bit, 8-Bit, 12-Bit, and 16-Bit segment bit-depth) but with fixed gray scale bit-depth (3-Bit gray scale).

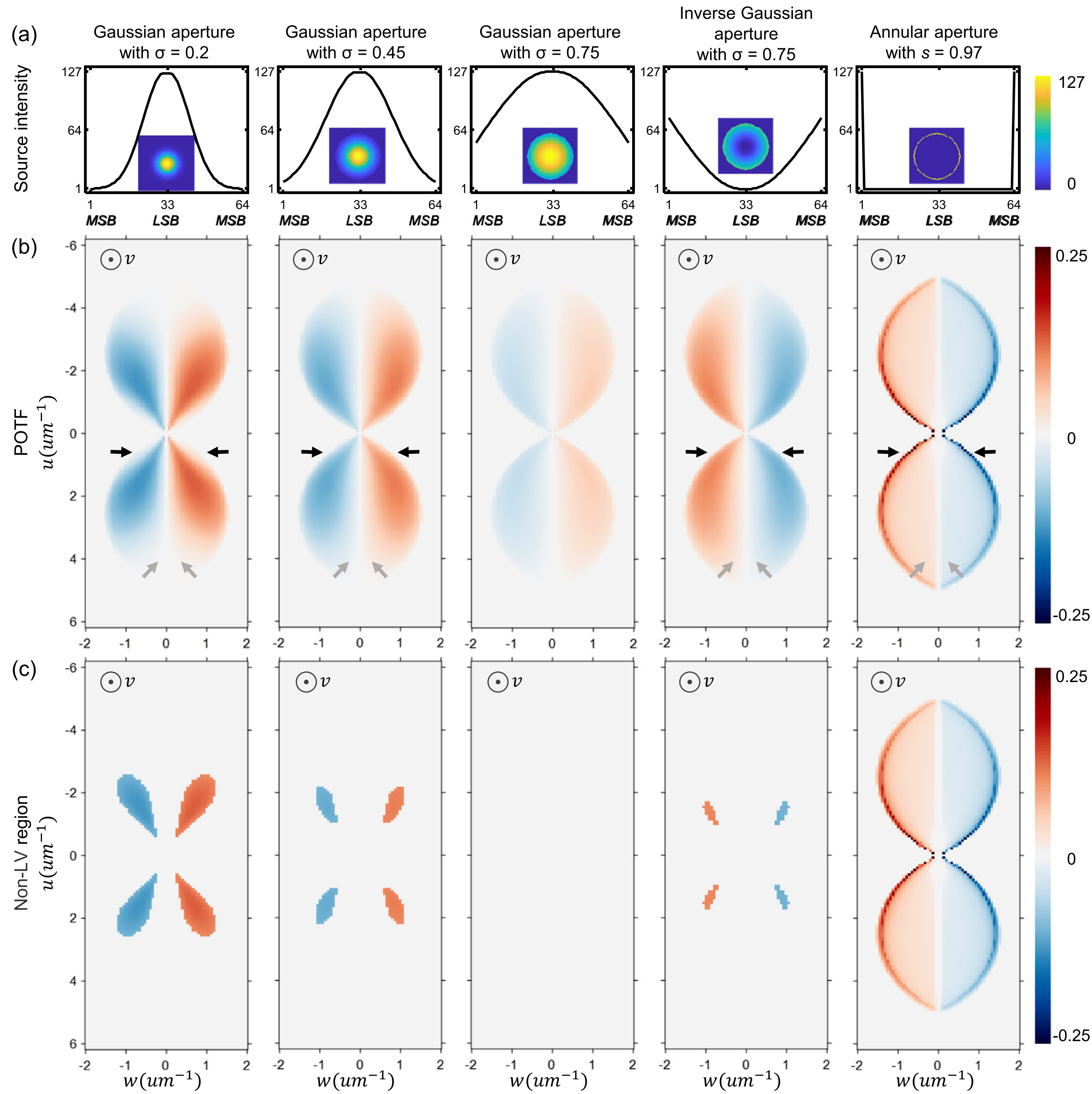

Fig. 7. Characterization of 3D POTF for GIs and annular illumination with 32-Bit segment bit-depth with 8-Bit gray bit-depth. (a) GI apertures with different standard deviations ($\sigma = 0.25$, $\sigma = 0.45$ and $\sigma = 0.75$), an inverse GI with 0.75 deviations value, and an annular illumination with coherent parameter $s = 0.97$. (b)-(c) Corresponding section of 3D POTF and non-LV coverage region in $u - w$ plane of different GI sources and annular source. Missing cone region and high frequency missing region are marked by the black and gray arrows, respectively.

Bit segment with 8-Bit gray bit-depth are invoked for the GI with different standard deviations, as displayed in Fig. 7(a). The curve of Gaussian source pattern is composed with 32-Bit segment from MSB to LSB and 128 gray level, and the bit-depth of segmentation and gray scale discretization is basically enough for pupil coding engineering in this case. Fig. 7(a) displays the source intensity distribution and the corresponding illumination profiles projected on the condenser back focal plane with the maximum illumination NA ($NA_{ill} = 1.4$). Among the proposed illumination patterns, there are three GI apertures with different standard deviations ($\sigma = 0.25$, $\sigma = 0.45$ and $\sigma = 0.75$), an inverse GI with 0.75 deviations value, and an annular illumination with coherent parameter $s = 0.97$, respectively. As proposed in Fig. 7(b)-(c), the corresponding 3D POTF sections of different GIsources and annular source are plotted in $u - w$ plane, and the non-LV region of POTF sections are given as well. It should be noted that we do not normalized the range of POTF from -1 to 1, thus, the POTFs have different contrast in the fixed range in Fig. 7.

In the case of GI apertures, the standard deviations of Gaussian pattern changes from 0.2 to 0.75, and the contrast of transfer function is decreased with the increasing of deviations value. However, the coverage of missing cone region marked by the black arrows as well as the high frequency region marked by the gray arrows are getting smaller with bigger deviations value in Fig. 7(b). The MSB of illumination segments corresponding high NA are accompanied by wider POTF frequency coverage area, but the frequency component contributions of low NA (LSB) and high NA (MSB) cancel each other resulting large missing cone region and weak contrast of POTF response. This contrast reducing phenomenon is reflected in the non-LV region plots of GI where the POTF contribution of LV values are almost negligible, and the non-LV coverage is getting smaller as well. For the comparison of POTF between the GI and inverse GI with the same 0.75 deviation value, the absolute POTF distributions of these two illumination apertures are totally same with each other except for a linear factor of POTF according to the incoherent superposition theory of POTF. This linear factor is basically related to the source intensity area and equals to the source area ratio of two completely complementary illumination sources (sum of these two complementary sources intensity area equals 1). The corresponding POTF of annular pattern has the strongest contrast among the POTFs in Fig. 7, in particular, the frequency components with relatively large value are mainly distributed on the Ewald sphere of outer boundary due to the robust frequency response contribution of MSB among small source intensity area. Regardless of the various apertures, there always exists a missing cone frequency region around the axis creating artifacts such as halos and longitudinal stretching in the reconstructed 3D object in both C-ODT and PC-ODT modalities, and it is a well-known drawback of the wide-field microscopy. Note that the regularization parameter plays a crucial role in the deconvolution process of 3D POTF by invoking the Wiener deconvolution algorithm [28,42]. In practice, the value of regularization parameter is unknown and spatial-frequency dependent variable, and this value have to be carefully estimated for each spatial frequency region of the POTF. In order to avoid the effect of regularization parameter to final 3D RI reconstruction, the same regularization parameter is utilized for the POTFs deconvolution of presented simulated and experimental sources to ensure the minimal limitations of regularization parameter in the analysis of illumination patterns.

Besides, we simulate a pure phase micro sphere under different GI apertures and annular aperture to analyse the imaging SNR performance of various POTFs. This ideal phase micro bead (bead diameter $D_{bead} = 3$ μm, bead RI $n_{bead} = 1.59$) is a homogeneous structure and it is immersed in a surrounding medium mimicking the RI matching oil (Medium RI $n_m = 1.58$). Note that the system parameters (Maximum $NA_{ill} = NA_{obj} = 1.4$, central wavelength $\lambda = 550$ nm) invoked in this simulation are same with the 3D POTF calculation in the above section, as well as the parameter of actual experimental setup. The intensity stack of each corresponding illumination source contains 256 × 256 × 256 pixels, and the lateral and axial sampling rates are both 0.065 μm.

Fig. 8 shows the comparative reconstruction results of the 3D phase bead, and the first two rows of Fig. 8 are the simulated bead intensity stack sections and Fourier spectrum sections under the white Gaussian noise with different standard deviations ($\sigma_{noise} = 0.1$ and $\sigma_{noise} = 0.25$, respectively). The bead through-focus intensity data can be obtained by the convolution of corresponding PSF and ideal phase bead and the addition of random noise. It can be observed that the feature of Fourier spectrum becomes harder to resolve with larger noise deviation. Then, the middle two rows in Fig. 8 displays the recovered $x - y$ slice of the reconstructed bead RI under each illumination, and the corresponding deconvolved Fourier spectrum section.

By analyzing the RI sections shown in Fig. 8, we observe that GI with larger deviation value σ provides better axial imaging results, but the recovered RI contrast is decreased. Thus, the GI with $\sigma = 0.75$ has the worst contrast of the bead RI structure, while the RI distribution obtained for annular illumination is more uniform than that of the other illuminations. Furthermore, more robust SNR RI results of annular pattern validates that the annular source pattern can provide the best performance among the illuminations. Moreover, the lateral and axial RI Profiles of recovered bead are plotted in the last two rows of Fig. 8 to give more intuitive results about the characteristics of each illumination aperture. Compared with the ideal lateral and axial bead RI profile (marked by solid and dotted red line, respectively), the lateral RI profiles under deviation of 0.1 (marked by solid green line) and deviation of 0.25 (marked by solid blue line) noise can provide relatively good imaging results. The axial imaging RI profiles (marked by dotted green and blue line, respectively) are getting better with the increasing of sigma value, but the noise fluctuation of line profile under deviation 0.25 noise addition. In contrast, the annular illumination aperture can effectively suppress the noise under different noise conditions and maintain relatively high SNR of the RI reconstruction. From these results, it can be concluded that the annular aperture is the optimal illumination pattern theoretically and corresponding POTF can provide the best imaging performance compared with GI strategy.

3. System Setup

The proposed optimization analysis of illumination aperture is built on an inverted commercial microscope (IX83, Olympus), as depicted in Fig. 9. A halogen white light source with a green interference filter is used for illumination, which can provide quasi-monochromatic lights with narrow bandwidth (central wavelength $\lambda_0 = 550$ nm, ∼10 nm bandwidth). All experiments in the text were conducted using a 100 × oil-immersion microscope objective (Olympus UPLSAPO, NA = 1.4) and an oil-immersion condenser type top lens (Olympus, NA = 1.4, $n_{oil} = 1.515$, maximum incident angle = 67.5°). Images were taken with an sCMOS camera (Hamamatsu, Orca Flash 4.0 V3, 6.5 μm pixel pitch). The GI and annular illumination patterns used in this work are custom-printed on circular film flakes with the opaque regions, and these aperture filters are designed with different spatial parameters. The standard deviations of GI patterns are 0.2, 0.45, and 0.75, respectively, and the normalized radius of central opaque circular region of angular pattern is 0.9 corresponding to coherence parameter. Moreover, the custom-printed gray film flake aperture is placed in the gap between two thin circular glass plates, and all illumination apertures are manually fitted into an open slot positions in the condenser turret and properly centered in the optical pathway. The axial scanning of intensity stack is realized by a mechanical motorized refocusing system (e.g., piezo-stage) with a step size of 0.065 μm providing the same sampling rate with lateral direction.

In our case, four sets of data are measured under corresponding illumination apertures, and the spatial sampling rates for these intensity stacks in x, y and z directions are both 0.065 μm. As for the image acquisition and data processing time in our experiments, the exposure times are set to 15 ms for GI aperture with $\sigma = 0.2$, 10 ms for GI aperture with $\sigma = 0.45$, 5 ms for GI aperture with $\sigma = 0.75$, and 30 ms for annular illumination aperture with $s = 0.9$, respectively. All the experimental data is processed in a workstation (Intel Core i7-7820X, 3.6 GHz, 64 GB DDR4 RAM), and the time required for all computation processes (Parallel stack deconvolution operations) of intensity stacks field of view (FOV) (401 × 401 × 401 × 4) is about 6 seconds.

4. Results

4.1. Comparative result on control bead sample

To demonstrate the RI imaging performance of several illumination apertures proposed in the simulation section, we implement the experiments on control bead sample and the comparative experimental results are illustrated in Fig. 10. The control sample is the micro polystyrene bead (Polysciences, $n = 1.59$ at $\lambda_0 = 589$ nm) with 6 μm diameters immersed in RI matching oil (Cargille, $n_m = 1.58$). For this experiment, the detailed parameters are same with the simulation in subsection 2.4 expect that the dimension of captured intensity stack is 401 × 401 × 401. Fig. 10 displays the comparative intensity sections, POTF sections, and Fourier spectrum sections of micro phase bead under types of apertures, and the final RI section reconstruction results are presented as well. In the first row of Fig. 10, we show the axial raw intensity of phase bead

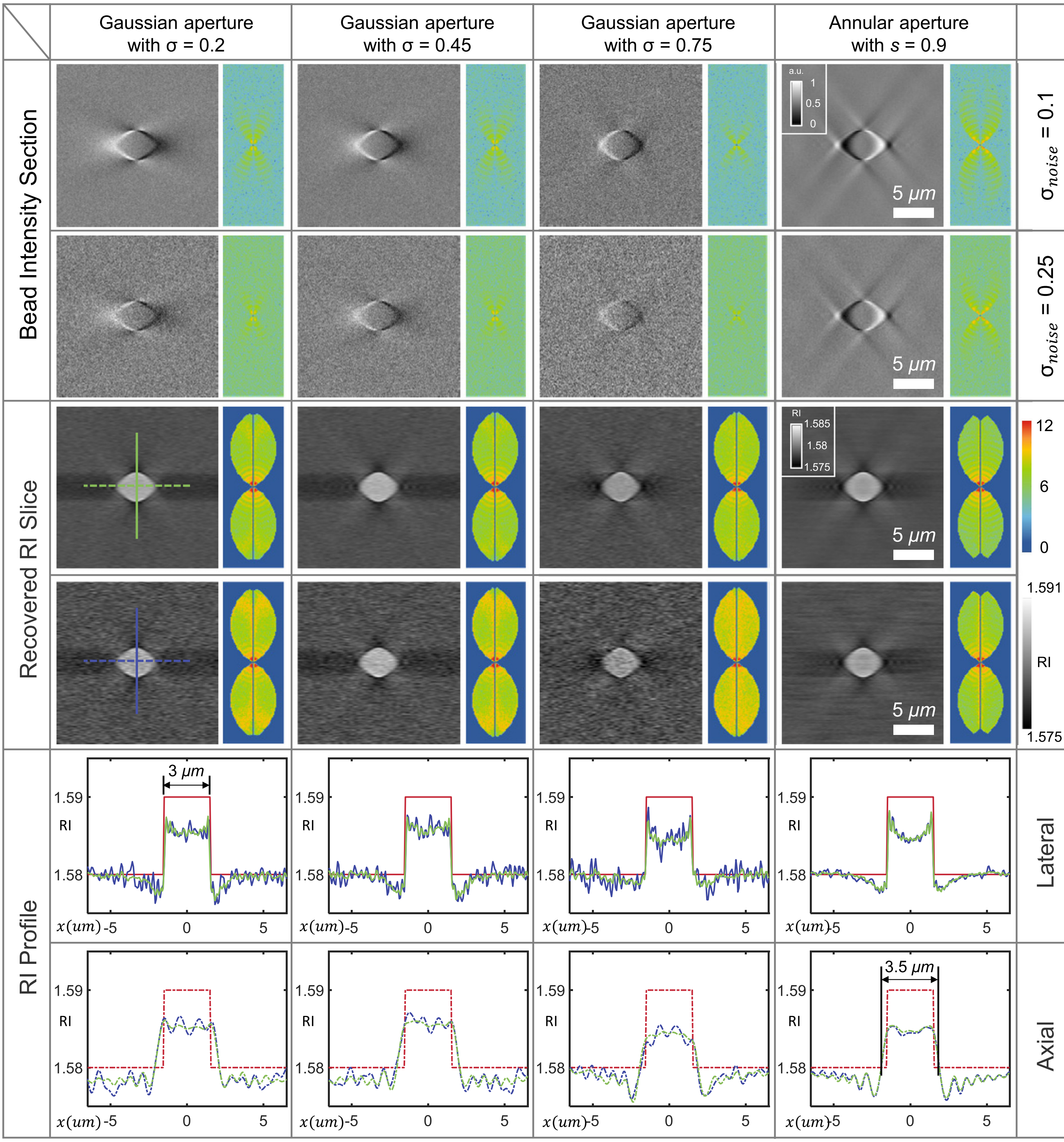

Fig. 8. Simulation results based on a pure phase micro sphere under different GI apertures and annular aperture for the imaging SNR performance analysis of various POTFs. Theoretical lateral and axial bead RI profile are indicated by solid and dotted red line, respectively. Lateral RI profiles under deviations of 0.1 and 0.25 noise are marked by solid green and blue lines, respectively. Axial imaging RI profiles are marked by dotted green and blue lines, respectively.

for Gaussian aperture with standard deviation $\sigma = 0.2$, $\sigma = 0.45$, $\sigma = 0.75$, and annular aperture with $s = 0.9$, respectively. All intensity stack sets are normalized to same background eliminating the effect of source brightness and exposure time. It is intuitive that the intensity contrast is vanished gradually under Gaussian aperture with the increase of deviation value, while the intensity section under annular illumination still provides relatively strong contrast. Besides, the POTF and Fourier spectrum slices of corresponding illumination aperture are provided in the second row of Fig. 10. The shape and the amplitude distribution of POTF and Fourier spectrum are consistent with each other, and the envelope of incoherent POTF is also indicated by the white dotted line.

We can observe that the missing cone region inside the envelope (indicated by the gray arrows) is gradually decreasing, while the low frequency amplitude contrast becomes weak simultaneously. The missing cone region marked by the white arrows is induced by the limited illumination angle, and the frequency components in the Fourier spectrum of each intensity stack are matched well with the corresponding POTF both in shape and amplitude. The last three rows of Fig. 10 illustrate the re-

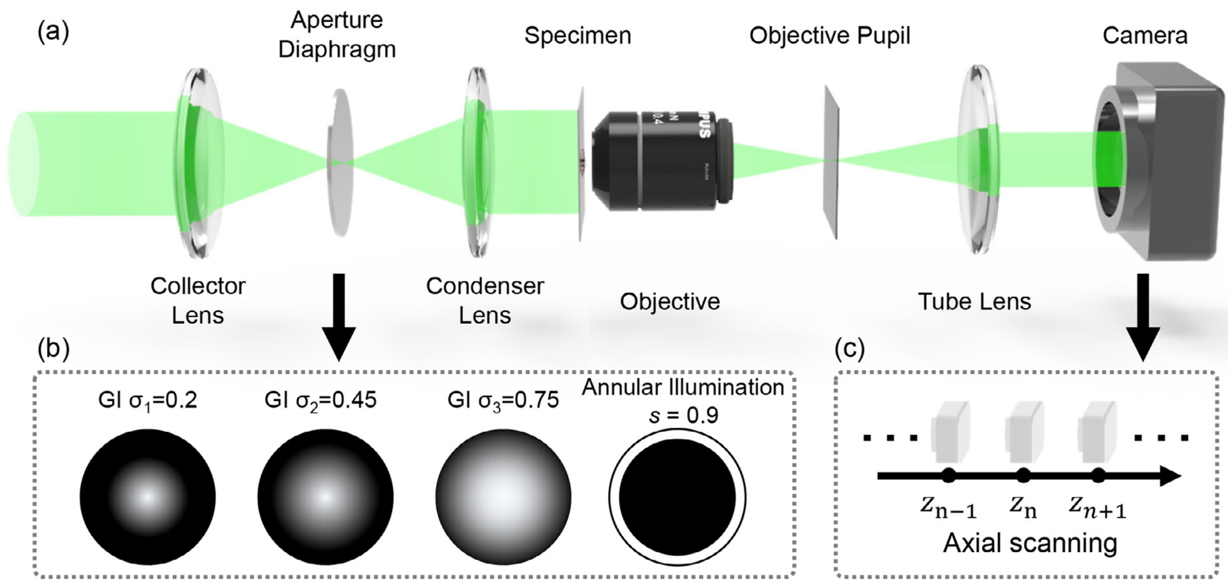

Fig. 9. Schematic illustration of experimental setup. (a) Description of partially coherent microscope. (b) Aperture diaphragm before the condenser lens can be custom-designed to the Gaussian and annular shaped aperture in the condenser turret. (c) Intensity stacks are recorded under respective illumination pattern.

covered RI slice alone axial and lateral directions. This result shows the conclusion that the increasing of deviation value of Gaussian aperture is helpful to improve the axial imaging resolution of tomography, but it will vanish the response amplitude of POTF at low frequency. Above phenomenon is similar to the effect of coherence parameter for circular illuminator aperture between resolution and contrast in bright-field microscope. On the contrary, the annular illumination not only provide relatively strong intensity contrast but also cover the whole frequency pass-band. It should be noted that the recovered bead RI distribution under the annular illumination pattern is a little bit distorted, and the mismatch of shape and RI value between experimental and ideal distribution is caused by the misalignments of annular illumination and objective. This means that the position alignment tolerance of GI aperture is better than annular illumination because the annular illumination only containing non-paraxially high illumination angle in experiments even though the theoretical performance of annular illumination is the optimal among all combinations of gray scale illumination patterns. Indeed, the lateral imaging performance is not much different expecting lower axial resolution, but the annular illumination is easily disturbed by the aliment error to the objective pupil compared with GI pattern and circular illumination pattern.

4.2. Comparative result on unstained biological cell

Moreover, we test these illumination apertures on the unstained biological cell sample and evaluate the RI imaging capability of various apertures in its intended biomedical applications. A clusters of unstained human breast cancer MCF-7 cell is distributed on a glass sample slide with 0.9% sodium chloride immersion matching medium ($n_{water} = 1.33$), and a thin *no*. 0 coverslip is placed on the top of sample. For the case where the RI of sample immersion medium is smaller than the RI of objective immersion medium, the illumination NA may not match with the surrounding medium RI and, this mismatch will cause the the shrinking of effective illumination NA smaller than the actual NA of condenser lenses. Within the volume of 301 × 301 × 301 pixels, the recovered region is about 20 × 20 × 20 μm^3 with sampling rate of 0.065 μm along lateral and axial directions. Fig. 11 displays the detailed comparison of 3D RI results on unstained MCF-7 cell. The experimental results of lateral intensity sections, axial Fourier spectrum sections, and the recovered RI slices are proposed. In the first row of Fig. 11, the cell intensity stack sections in the central planes are presented. Similarly, it can be observed that the image contrast becomes weaker with larger deviation for GI, and the intensity cross section of annular illumination pattern still maintain a high level of contrast. The Fourier spectrum sections of captured intensity stack and recovered Fourier spectrum of RI stack are coincident with POTF both in shape and distribution for corresponding illumination patterns, which is same with the previously observed simulation and experiment phenomena illustrated in Fig. 8 and Fig. 10.

In addition, the comparisons of RI reconstruction are provided in Fig. 11 demonstrating the differences in imaging performance of various illumination apertures. The axial RI slices locating at $x1 = 1.82$ μm illustrate the changing of RI contrast and the axial imaging resolution, just like the prolongation of cell's nuclei marked with white solid ellipses. The GI pattern with the smallest deviation value can give relatively strong reconstruction contrast but with the worse axial resection. While the axial RI slice of annular illumination pattern can provide high contrast as well as the best axial imaging resolution among these illumination apertures. The images of RI reconstruction at three different lateral planes ($z1$ = -2.47 μm, $z2$ = -0.91 μm, $z3$ = 0.39 μm) are selected to compare the imaging ability of theses illumination aperture. Within these lateral RI slices, the cellular membrane folds and cell boundaries with high RI contrast and high resolution (marked with red arrows) is observed. The fine subcellular structures including nuclei and organelle are also visible and well resolved across multiple reconstructed $x - y$ slices (marked with green and blue arrows). In the $x - y$ cross-sectional views, some tiny grains feature in cytoplasm appeared brighter and sharper contrast are reconstructed with higher refractive index values in cytoplasm (indicated with solid and dotted circles). Thus, from the comparative result on unstained biological cell, the Gaussian aperture with smaller deviation value provides robust low frequency SNR but the axial resolution is limited, while the POTF of annular illumination has better axial imaging ability and relatively strong intensity contrast.

5. Conclusion and discussion

In summary, we propose a gray scale segment division and coding scheme for illumination based on conventional bright-field microscope, and the optimality of POTF corresponding annular illumination source is demonstrated for single partially coherent aperture illumination in 3D diffraction tomography. And this is the first time to present the

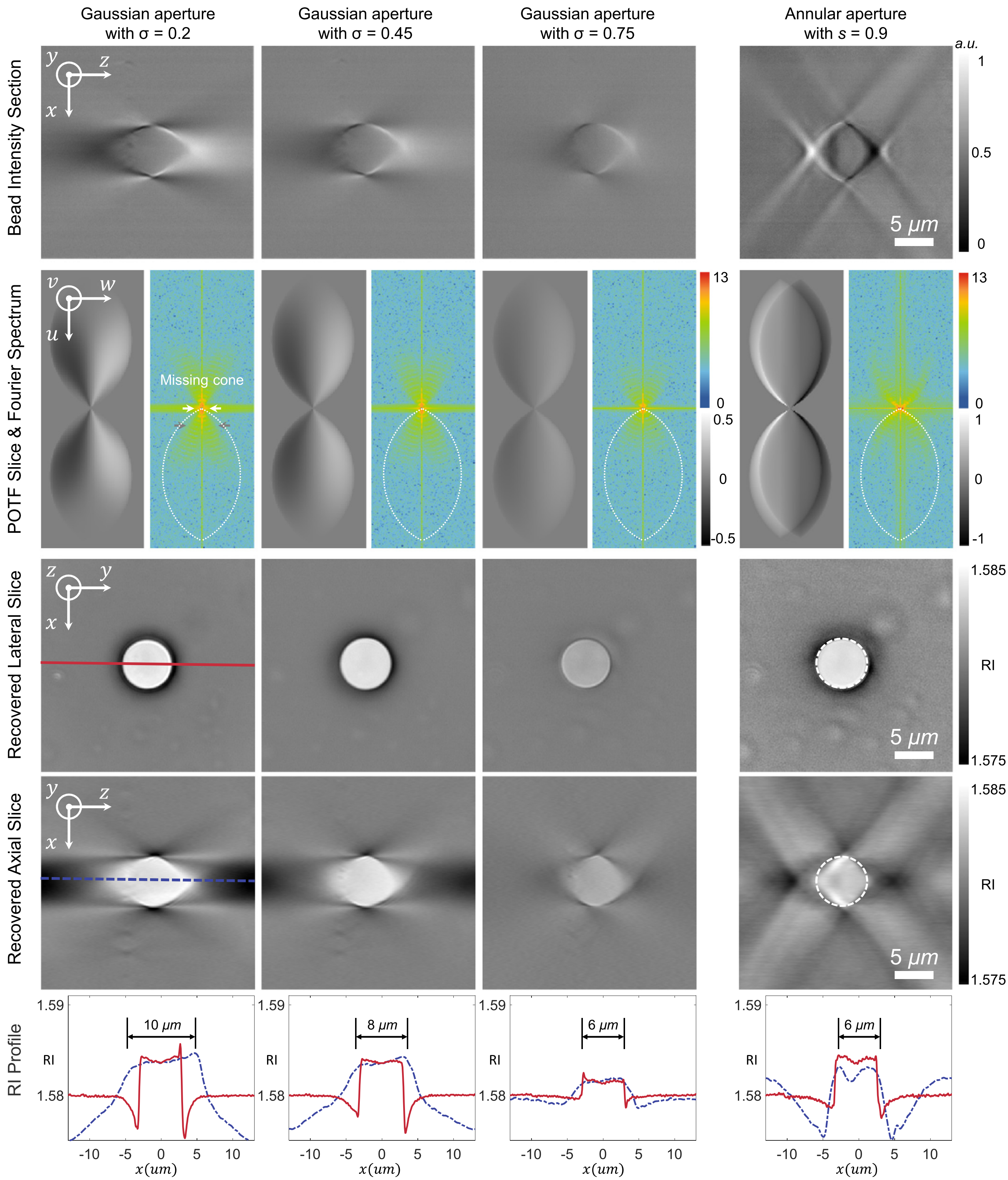

Fig. 10. Experimental comparison results on control bead sample under different GI patterns and annular illumination pattern. Axial intensity sections, POTF sections, and Fourier spectrum sections of micro phase bead under types of apertures is displayed. The final recovered lateral slices, axial slices, and the RI Profiles are presented as well. The missing cone region is indicated by the arrows (white and gray). White dotted circles indicate exact profile of micro bead.

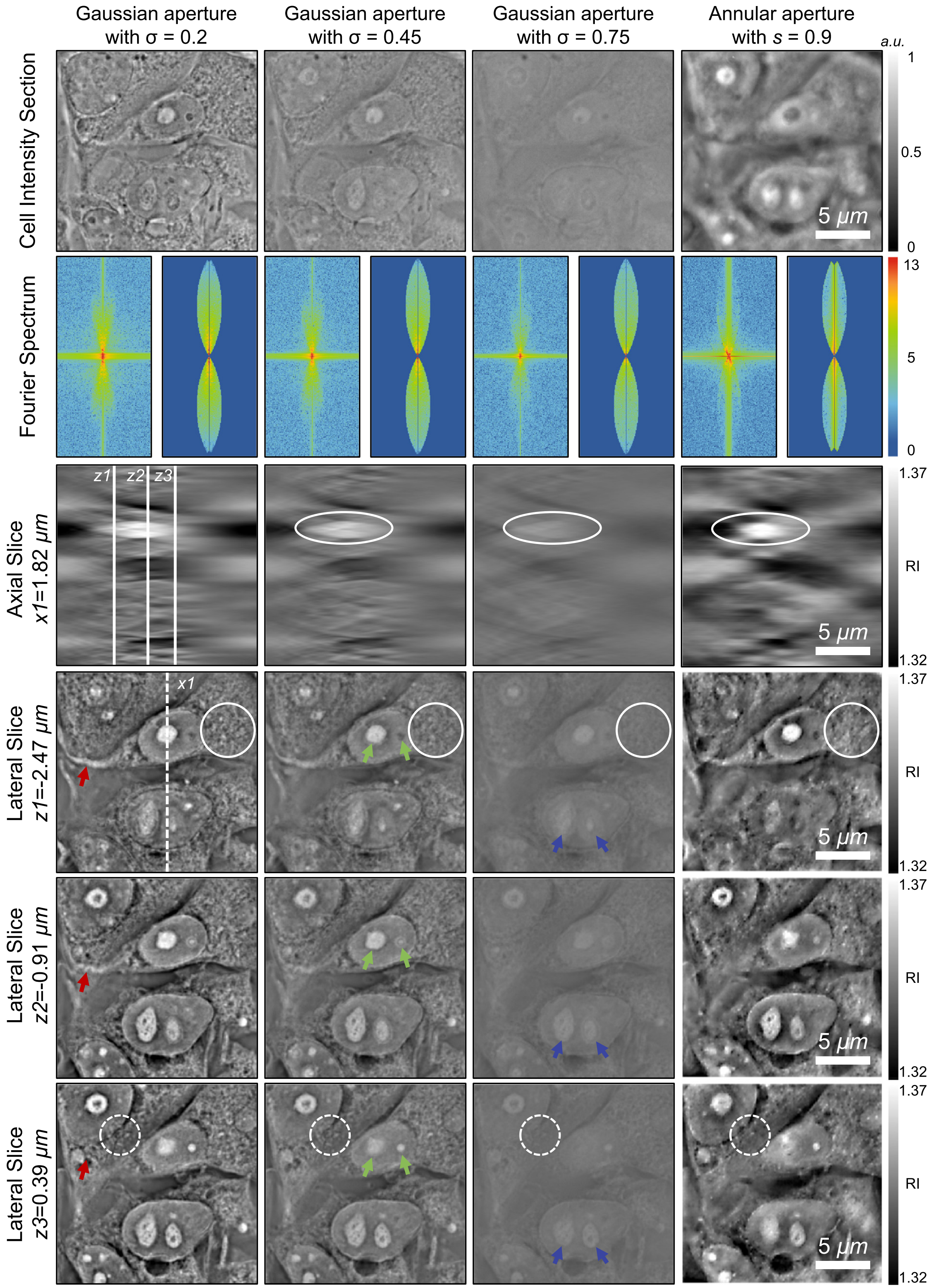

Fig. 11. Tomographic reconstruction of unstained human breast cancer MCF-7 cell. The central lateral sections of cell intensity, Fourier spectrum sections of intensity stack, and recovered Fourier spectrum sections of RI are proposed. Besides, RI reconstructions at axial and different lateral planes ($x1$ = 1.82 μm, $z1$ = -2.47 μm, $z2$ = -0.91 μm, $z3$ = 0.39 μm) are demonstrated. The axial distribution of cell's nuclei is prolonged (indicated by the white ellipses). The fine subcellular structures including cellular membrane folds, nuclei, and organelle (marked with red, green, and blue arrows, respectively) and some tiny grains feature in cytoplasm appeared brighter and sharper RI contrast (indicated with solid and dotted circles) are distinguishable and well resolved across multiple reconstructed slices.

theoretical optimization analysis of 3D POTF in PC-ODT among arbitrary illuminations instead of focusing only on Gaussian patterns. The coding of arbitrary gray illumination pattern index makes it easier to calculate the POTF and evaluate the quality of POTF. Also, the custom-build quantitative metrics is introduced to maximize the performance of POTF related to the "goodness" evaluation of an illumination aperture, and the optimal illumination aperture with the imaging performance of POTF is selected. Further, the optimal illumination strategy and analysis are implemented on a simulated micro phase bead object, and the experimental results based on a real control bead sample and unstained MCF-7 cell clusters demonstrate the best POTF quality of annular illumination among proposed various source patten. The proposed work enables new promising directions in biological cell studies and versatile applications in biological and biomedical research in 3D RI tomographic imaging.

Note that there are still some issues should be discussed in this section. The analytical approach of POTF calculation is much faster and equally accurate compared to numerical integration methods that integrate over a series of segment annuli, but the analytical express is not available for some complex non-uniform illuminations containing high order polynomial term. Thus, the POTF has been numerically calculated in this manuscript and its theoretically optimal design has been investigated by a commonly used numerical process instead of a brute-force one. Even though we found that the absolute brightness of illumination source does not affect the distribution POTF of system and a thin annular ring matched with objective NA was determined to be the best illumination source, the annular illumination scheme may not be the most effective in the realistic experimental setup due to the SNR and misalignment of real imaging model.

Actually, the brightness of annular illumination will cause bad SNR of image in realistic digital imaging process. Moreover, the misalignment of imaging system between the objective and illumination aperture is not taken into consideration, and the mismatch between the theoretical and experimental 3D POTF of annular source may cause severe artifacts in RI reconstruction and degrade the imaging resolution. In spite that the annular illumination pattern may not the best one in PC-ODT experiments, we demonstrate the optimal illumination scheme under theoretically ideal situation. The modeling and characterization of realistic experiments for 3D RI reconstruction (including misalignment and noise in imaging system) is beyond the scope of this work. For the left issues, more accurate realistic model including noise to single characterization, aperture alignment tolerance analysis, and finer programmable gray scale source (e.g., micro LED and organic LED) should be explored in the future work. A future line in the development of post-deconvolution processing will be investigated as well.

Funding

National Natural Science Foundation of China (61722506, 61905115), Leading Technology of Jiangsu Basic Research Plan (BK20192003), National Defense Science and Technology Foundation of China (2019-JCJQ-JJ-381), Youth Foundation of Jiangsu Province (BK20190445), The Key Research and Development Program of Jiangsu Province (BE2017162), "333 Engineering" Research Project of Jiangsu Province (BRA2016407), Fundamental Research Funds for the Central Universities (30920032101), and Open Research Fund of Jiangsu Key Laboratory of Spectral Imaging & Intelligent Sense (3091801410411).

Declaration of Competing Interest

The authors declare that they have no known competing financial interests or personal relationships that could have appeared to influence the work reported in the paper entitled "Optimization analysis of partially coherent illumination for refractive index tomographic microscopy".

Supplementary material

Supplementary material associated with this article can be found, in the online version, at 10.1016/j.optlaseng.2021.106624

CRediT authorship contribution statement

Jiaji Li: Conceptualization, Data curation, Formal analysis, Methodology, Investigation, Validation, Visualization, Writing - original draft. **Ning Zhou:** Formal analysis, Writing - original draft. **Zhidong Bai:** Writing - original draft. **Shun Zhou:** Writing - original draft. **Qian Chen:** Supervision, Funding acquisition, Writing - original draft. **Chao Zuo:** Supervision, Funding acquisition, Writing - original draft.

References

[1] Choi W, Fang-Yen C, Badizadegan K, Oh S, Lue N, Dasari RR, Feld MS. Tomographic phase microscopy. Nat Methods 2007;4:717–19.
[2] Park Y, Diez-Silva M, Popescu G, Lykotrafitis G, Choi W, Feld MS, Suresh S. Refractive index maps and membrane dynamics of human red blood cells parasitized by plasmodium falciparum. In: Proceedings of the National Academy of Sciences, vol. 105; 2008. p. 13730–5.
[3] Park Y, Depeursinge C, Popescu G. Quantitative phase imaging in biomedicine. Nature Photonics 2018;12:578.
[4] Zuo C, Li J, Sun J, Fan Y, Zhang J, Lu L, Zhang R, Wang B, Huang L, Chen Q. Transport of intensity equation: a tutorial. Optics and Lasers in Engineering 2020:106187.
[5] Zucker R.M.. Whole insect and mammalian embryo imaging with confocal microscopy: morphology and apoptosis. 2006. Cytometry Part A: The Journal of the International Society for Analytical Cytology, 69, 1143–1152.
[6] Zipfel WR, Williams RM, Webb WW. Nonlinear magic: multiphoton microscopy in the biosciences. Nature Biotechnology 2003;21:1369–77.
[7] Stephens DJ, Allan VJ. Light microscopy techniques for live cell imaging. Science 2003;300:82–6.
[8] Hoebe R, Oven CV, Gadella TJ, Dhonukshe P, Noorden CV, Manders E. Controlled light-exposure microscopy reduces photobleaching and phototoxicity in fluorescence live-cell imaging. Nature Biotechnology 2007;25:249–53.
[9] Wäldchen S, Lehmann J, Klein T, Van De Linde S, Sauer M. Light-induced cell damage in live-cell super-resolution microscopy. Scientific reports 2015;5(1):1–12.
[10] Nguyen TH, Kandel ME, Rubessa M, Wheeler MB, Popescu G. Gradient light interference microscopy for 3D imaging of unlabeled specimens. Nature Communications 2017;8:210.
[11] Sung Y, Choi W, Fang-Yen C, Badizadegan K, Dasari RR, Feld MS. Optical diffraction tomography for high resolution live cell imaging. Opt Express 2009;17:266–77.
[12] Cotte Y, Toy F, Jourdain P, Pavillon N, Boss D, Magistretti P, Marquet P, Depeursinge C. Marker-free phase nanoscopy. Nature Photonics 2013.
[13] Kim Y, Shim H, Kim K, Park H, Heo JH, Yoon J, et al. Common-path diffraction optical tomography for investigation of three-dimensional structures and dynamics of biological cells. Optics Express 2014;22:10398–407.
[14] Yoon J, Kim K, Park H, Choi C, Jang S, Park Y. Label-free characterization of white blood cells by measuring 3d refractive index maps. Biomedical optics express 2015;6:3865–75.
[15] Krauze W, Kuś A, Śladowski D, Skrzypek E, Kujawińska M. Reconstruction method for extended depth-of-field optical diffraction tomography. Methods 2018;136:40–9.
[16] Kuś A, Krauze W, Kujawińska M. Limited-angle holographic tomography with optically controlled projection generation. In: Three-Dimensional and Multidimensional Microscopy. Image Acquisition and Processing, XXII; vol 9330 9330079330. International Society for Optics and Photonics; 2015.
[17] Shin S, Kim K, Yoon J, Park Y. Active illumination using a digital micromirror device for quantitative phase imaging. Optics Letters 2015;40:5407–10.
[18] Lee K, Kim K, Kim G, Shin S, Park Y. Time-multiplexed structured illumination using a dmd for optical diffraction tomography. Optics letters 2017;42:999–1002.
[19] Merola F, Memmolo P, Miccio L, Savoia R, Mugnano M, Fontana A, D'ippolito G, Sardo A, Iolascon A, Gambale A. Tomographic flow cytometry by digital holography. Light: Science & Applications 2017;6. e16241–e16241
[20] Kuś A, Dudek M, Kemper B, Kujawińska M, Vollmer A. Tomographic phase microscopy of living three-dimensional cell cultures. Journal of Biomedical Optics 2014;19 046009–046009.
[21] Kak A.C., Slaney M., Wang G.. Principles of computerized tomographic imaging. 2002.
[22] Wolf E. Three-dimensional structure determination of semi-transparent objects from holographic data. Opt. Commun. 1969;1:153–6.
[23] Lauer V. New approach to optical diffraction tomography yielding a vector equation of diffraction tomography and a novel tomographic microscope. J. Microsc 2002;205:165–76.
[24] Horstmeyer R, Chung J, Ou X, Zheng G, Yang C. Diffraction tomography with fourier ptychography. Optica 2016;3:827–35.
[25] Rodrigo JA, Soto JM, Alieva T. Fast label-free microscopy technique for 3d dynamic quantitative imaging of living cells. Biomedical Optics Express 2017;8:5507–17.
[26] Soto JM, Rodrigo JA, Alieva T. Optical diffraction tomography with fully and partially coherent illumination in high numerical aperture label-free microscopy. Applied Optics 57 2018:A205–14.

[27] Li J, Chen Q, Zhang J, Zhang Z, Zhang Y, Zuo C. Optical diffraction tomography microscopy with transport of intensity equation using a light-emitting diode array. Optics and lasers in engineering 2017;95:26–34.
[28] Li J, Chen Q, Sun J, Zhang J, Ding J, Zuo C. Three-dimensional tomographic microscopy technique with multi-frequency combination with partially coherent illuminations. Biomedical optics express 2018;9:2526–42.
[29] Tian L, Wang J, Waller L. 3d differential phase-contrast microscopy with computational illumination using an led array. Optics letters 2014;39:1326–9.
[30] Tian L, Waller L. Quantitative differential phase contrast imaging in an LED array microscope. Opt Express 2015;23:11394–403.
[31] Ling R, Tahir W, Lin H-Y, Lee H, Tian L. High-throughput intensity diffraction tomography with a computational microscope. Biomedical Optics Express 2018;9:2130.
[32] Li J, Matlock A, Li Y, Chen Q, Zuo C, Tian L. High-speed in vitro intensity diffraction tomography. Advanced Photonics 2019;1:066004.
[33] Matlock A, Tian L. High-throughput, volumetric quantitative phase imaging with multiplexed intensity diffraction tomography. Biomedical Optics Express 2019;10:6432.
[34] Chowdhury S, Chen M, Eckert R, Ren D, Wu F, Repina N, Waller L. High-resolution 3d refractive index microscopy of multiple-scattering samples from intensity images. Optica 2019;6:1211–19.
[35] Li J, Matlock A, Li Y, Chen Q, Tian L, Zuo C. Resolution-enhanced intensity diffraction tomography in high numerical aperture label-free microscopy. Photon Res 2020;8:1818–26.
[36] Zheng G, Horstmeyer R, Yang C. Wide-field, high-resolution fourier ptychographic microscopy. Nature photonics 2013;7:739–45.
[37] Zheng G, Shen C, Jiang S, Song P, Yang C. Concept, implementations and applications of fourier ptychography. Nature Reviews Physics 2021:1–17.
[38] Zuo C, Sun J, Li J, Asundi A, Chen Q. Wide-field high-resolution 3d microscopy with fourier ptychographic diffraction tomography. Optics and Lasers in Engineering 2020;128:106003.
[39] Streibl N. Three-dimensional imaging by a microscope. JOSA A 1985;2:121–7.
[40] Jenkins MH, Gaylord TK. Three-dimensional quantitative phase imaging via tomographic deconvolution phase microscopy. Applied optics 2015;54:9213–27.
[41] Chen M, Tian L, Waller L. 3d differential phase contrast microscopy. Biomed. Opt. Express 2016;7:3940–50.
[42] Soto JM, Rodrigo JA, Alieva T. Label-free quantitative 3d tomographic imaging for partially coherent light microscopy. Optics Express 2017;25:15699–712.
[43] Bao Y, Gaylord TK. Quantitative phase imaging method based on an analytical nonparaxial partially coherent phase optical transfer function. JOSA A 2016;33:2125–36.
[44] Soto JM, Rodrigo JA, Alieva T. Partially coherent illumination engineering for enhanced refractive index tomography. Optics letters 2018;43:4699–702.
[45] Zuo C, Sun J, Li J, Zhang J, Asundi A, Chen Q. High-resolution transport-of-intensity quantitative phase microscopy with annular illumination. Scientific reports 2017;7:7654.
[46] Li J, Chen Q, Zhang J, Zhang Y, Lu L, Zuo C. Efficient quantitative phase microscopy using programmable annular led illumination. Biomedical optics express 2017;8:4687–705.
[47] Huang J, Bao Y, Gaylord TK. Three-dimensional phase optical transfer function in axially symmetric microscopic quantitative phase imaging. JOSA A 2020;37:1857–72.
[48] Hugonnet H, Lee M, Park Y. Optimizing illumination in three-dimensional deconvolution microscopy for accurate refractive index tomography. Optics Express 2021;29:6293–301.
[49] Huang J., Bao Y., Gaylord T.K.. Analytical phase optical transfer function for gaussian illumination and the optimized profiles. 2020b. arXiv preprint: 2012.05690.
[50] Li J, Chen Q, Sun J, Zhang J, Pan X, Zuo C. Optimal illumination pattern for transport-of-intensity quantitative phase microscopy. Optics express 2018;26:27599–614.
[51] Rodrigo JA, Soto JM, Alieva T. Fast label-free optical diffraction tomography compatible with conventional wide-field microscopes. In: Optical Methods for Inspection, Characterization, and Imaging of Biomaterials IV vol. 11060; 2019. p. 1106016. International Society for Optics and Photonics
[52] Noda T, Kawata S, Minami S. Three-dimensional phase contrast imaging by an annular illumination microscope. Applied optics 1990;29:3810–15.
[53] Noda T, Kawata S, Minami S. Three-dimensional phase-contrast imaging by a computed-tomography microscope. Applied optics 1992;31:670–4.